Study on *In-Situ* Nucleation, Growth Kinetics and Crystallographic Structure of Acicular Ferrite in X100 Pipeline Steel Welds

Xiaonan Qi[1,2] · Xiaonan Wang[1] · Xinjun Shen[1] · Pengcheng Huan[2] · Zhenguang Liu[3] · Hongshuang Di[2]

Abstract

Acicular ferrite has appeared in various low carbon microalloyed steel welds (e.g., laser-arc hybrid welds) due to its high grain boundary density and toughness. However, the transformation kinetics and crystallographic structure characteristics of acicular ferrite in laser-arc hybrid welds are still unclear. In this paper, the nucleation and growth kinetics of acicular ferrite in laser-metal active gas hybrid welds with different cooling rates (1–150 K/s) were investigated and their crystallographic characteristics were revealed from the perspective of variant. The result showed that acicular ferrite can nucleate at all the test cooling rates in weld metal, and the microstructure coexisting with acicular ferrite changes from polygonal ferrite and granular bainite with a low cooling rate to lath martensite with a high cooling rate. As the cooling rate increases, the phase transformation temperature of acicular ferrite decreased, and the phase transformation mode changed from partitioning local equilibrium to negligible partitioning local equilibrium. The variety of the phase transformation mode and the higher phase transformation driving force led to an increase in the growth rate of acicular ferrite. Compared with the bainite and martensite in the base metal, the acicular ferrite had the characteristics of light variant selection, uniformly distributed operating factor and small variant size, which resulted in high-density effective grain boundaries. To obtain more acicular ferrite, the cooling rate should be increased as much as possible on the premise that the phase transformation termination temperature was higher than the M_s.

Keywords Pipeline steel · Laser-MAG hybrid welds · Acicular ferrite · Variant selection · Crystallographic structure

1 Introduction

In recent years, acicular ferrite (AF) has attracted considerable attention due to its increasing presence in various welds of low carbon microalloyed steels, especially recently discovered in laser-metal active gas (MAG) hybrid welds [1–4]. Generally, ferrite nucleated within austenite grains is called AF and specific inclusions can induce intragranular

ferrite nucleation [5, 6]. AF nucleation is mainly affected by steel composition, austenite grain size, non-metallic inclusions and cooling rate [7]. As the chemical composition is determined, the composition of the inclusions is also determined. Due to the large size of prior austenitic grain (PAG) in almost all welds, the effect of PAG size on AF nucleation is not obvious. Therefore, the cooling rate is a key factor affecting the nucleation of AF.

Previously, based on thermal expansion experiments, Wang et al. [8] determined that the accelerated cooling rate was important for austenite transformation and the increase of cooling rate from 2 to 15 K/s promoted the ferrite nucleation. Zhou et al. [9] compared the in situ nucleation process of acicular ferrite at the cooling rate of 0.5 K/s and 1.5 K/s, the results showed that ferrite sheets prefer to nucleate on inclusions rather than grain boundaries at faster cooling rates. Yang et al. [10] showed that the nucleation temperature of ferrite decreased with increasing cooling rate, and polygonal ferrite and bainite were formed together with acicular ferrite. In previous studies, the cooling rate for

✉ Xinjun Shen
    xjshen88@suda.edu.cn

✉ Hongshuang Di
    dhshuang@mail.neu.edu.cn

1   School of Iron and Steel, Soochow University, Suzhou 215002, China

2   The State Key Laboratory of Rolling and Automation of Northeastern University, Shenyang 110819, China

3   School of Materials Science and Engineering, Jiangsu University of Science and Technology, Zhenjiang 212000, China

obtaining AF was low, so that the microstructure coexisting with AF nucleation was polygonal ferrite and bainite. The reason was that AF was mainly obtained in welding methods with low cooling rate, such as arc welding and gas shielded welding. However, in our previous study [11, 12], AF was also nucleated in laser-MAG hybrid welds coexisting with lath martensite, which was characterized by low heat input. Therefore, it is necessary to study the nucleation and phase transformation kinetics of AF at relatively high cooling rates.

The purpose of introducing acicular ferrite into the welds is to improve the impact toughness. Previous research has shown that acicular ferrite has a high density of effective grain boundaries that can improve toughness [13, 14]. Wang et al. [15] also showed that AF increased the proportion of high-angle grain boundary (HAGB) and decreased the effective grain size. Liu et al. [16] showed that in steels with a large amount of AF, the densities of both HAGBs and low-angle grain boundaries (LAGBs) were high. The explanation for the high density of grain boundaries in AF was still at the morphological and structural level, and the result was that it had a fine needle-like structure. However, there is no study to explain the phenomenon of high-density grain boundaries from the perspective of AF crystallographic structure. Wang et al. [8] showed that the grain boundary distribution of AF exhibited the characteristics of high on both sides and low in the middle, which was the distribution characteristic of the shear microstructure, indicating that the orientation relationship of AF was related to the austenite. Variant selection and pairing directly affected grain boundary density in sheared microstructure. Therefore, variant selection and pairing within AF is worth investigating.

Our previous studies investigated the evolution behavior of weld inclusions and introduced acicular ferrite into laser-MAG hybrid weld [11, 17]. At the same time, we studied the nucleation and toughening mechanism of acicular ferrite in laser-MAG hybrid weld. Based on the previous research, AF in the laser-MAG hybrid welds with different cooling rates were detected and characterized in this paper. The growth kinetics of acicular ferrite and its crystallographic characteristics were studied from the perspective of variant. This paper provides a research basis for variant selection and pairing of acicular ferrite microstructures.

2 Materials and Procedure

2.1 Materials and Welding Procedure

In this study, the experimental material was the base metal and laser-MAG hybrid welds of X100 pipeline steel. The welding process of laser-MAG hybrid welds was based on the results of our previous research (TI_{10} weld) [11],

as shown in Fig. 1a. The chemical compositions of the experimental steel and welding wire were determined by inductively coupled plasma-optical emission spectroscopy (ICP-OES) method and shown in Table 1. Welds and base metal were machined into cylindrical samples ($\varphi 3 \times 8$ mm and $\varphi 3 \times 4$ mm). The schematic diagram of the sampling position is shown in Fig. 1b. The samples were heated to 1623 K in DIL805 phase transformation instrument and cooled at different cooling rates (1–150 K/s). The continuous cooling transformation (CCT) diagrams of welds and base metal were obtained according to the statistical results of the starting and ending temperatures of transformation and the proportion of microstructure. The samples were subjected to the same heat treatment process in high temperature laser scanning confocal microscopy (HT-LSCM) to obtain in situ information of AF nucleation. The HT-LSCM took ten photographs per second to observe nucleation and growth of acicular ferrite.

2.2 Microstructure Characterization

After HT-LSCM test, the specimens were prepared by mechanical polishing followed by etching with a 4% nital solution. We used BX53MRF Olympus metallographic microscope (OM), scanning electron microscope (SEM), Tecnai G2 F20 transmission electron microscope (TEM), and electron backscattered diffraction (EBSD) with the step size of 0.25 μm to characterize the microstructure and crystallographic structure. Image-Pro Plus 6.0 software was used to count the proportion of the microstructure. Channel 5 and Argpe software were used for postprocessing orientation data [18]. Inclusion evolution in the welds during solidification and the phase transformation points of welds were determined using Thermo-Calc software with the TCFE 9 database.

3 Results

3.1 *In-Situ* Observation of AF Nucleation and Microstructure Characterization

Figure 2 presents the results of AF nucleation at different cooling rates. Ferrite side plate (FSP) was first nucleated on grain boundaries at 1 K/s, as indicated by green rectangles in Fig. 2a. When the temperature decreased to ~847 K, interlocked AF nucleated around specific inclusions and grew in multiple directions was observed, as indicated by yellow circles in Fig. 2b. As the temperature was further decreased to ~786 K, the phase transformation stopped, as shown in Fig. 2c. The microstructure was mainly composed of AF and FSP. Figure 2d–j show the *in-situ* images of the weld microstructure at 10 K/s and 30 K/s, respectively. Microstructural

Fig. 1 Schematic diagram of test equipment and sampling **a** schematic diagram of welding equipment; **b** schematic diagram of sampling position; **c** schematic diagram of a high temperature confocal microscope
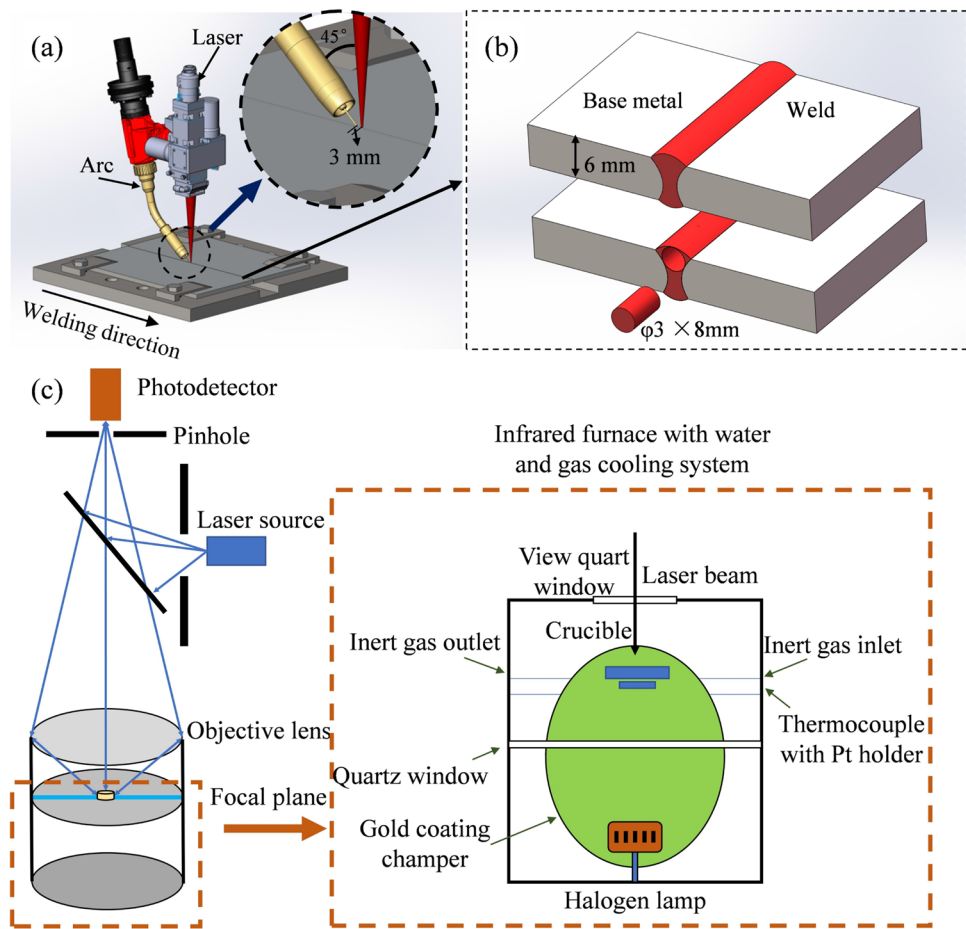

Table 1 Chemical compositions of the experimental steel and weld metal (wt %)

Element	C	Si	Mn	Cr	Ni	Mo	Cu	Al	Ti+Nb	S	Fe
Base metal	0.05	0.25	1.87	0.31	0.34	0.27	0.26	0.027	0.093	0.093	Bal
Weld metal	0.056	0.30	1.80	0.30	0.47	0.3	0.27	0.027	0.15	0.005	Bal

evolution of them was similar to the cooling rate of 1 K/s. FSP and AF nucleated and grew at prior austenite grain boundary (PAGB) and inclusions, respectively. The onset transformation temperature decreased with increasing cooling rate. Figure 2j–l show the *in-situ* images of the weld microstructure at 150 K/s. It was observed that FSP was no longer formed. The formation temperature of AF was further reduced to 862 K, and lath martensite (LM) was formed at 477 K, as shown in the red box in Fig. 2k. Finally, the microstructure was mainly composed of AF and LM. For comparison, Fig. 2m–o show the *in-situ* images of the base metal at 30 K/s. The lath bainite (LB) formed at 766 K nucleated and grew intragranular from the PAGB. LM formed at a lower temperature of 717 K, finally obtaining a mixed microstructure of LB and LM. The starting transformation temperature of the base metal was lower and the ending transformation temperature is higher than the welds.

Figure 3a–l presents microstructure of welds and base metals at different cooling rates. For weld metal, the microstructure was composed of mostly FSP and a small amount of AF (Fig. 3a, e) at the cooling rate of 1 K/s. At cooling rates of 10 K/s and 30 K/s, the microstructure was composed of mostly AF and a small fraction of FSP and granular bainite (GB), where AF nucleated from inclusion sites (Fig. 3b, f). At a cooling rate of 150 K/s, the microstructure was composed of AF and LM. For the base metal, with increasing cooling rate, the microstructure transformed from FSP to GB and LB, and finally to LM, which is consistent with previous studies [19–21].

Figure 3m shows the statistical results of PAGB at different cooling rates. Under different cooling rates, the PAGB size of the welds was basically the same (~50 μm). During the welding thermal cycle, the PAG size was mainly related to the peak temperature and high
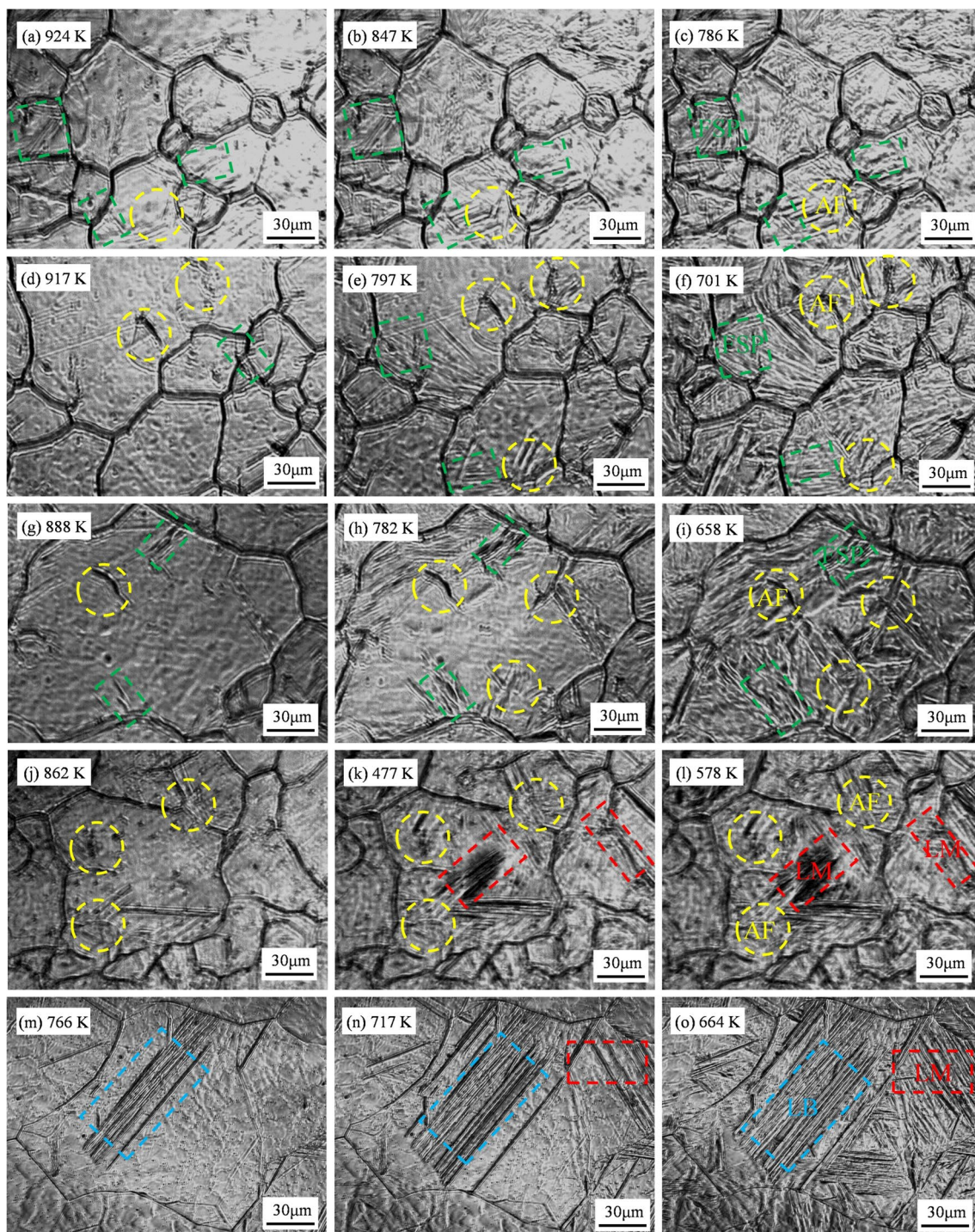
Fig. 2 In-situ images of microstructure nucleation and growth at different cooling rates **a–c** WM (weld metal)-1 K/s, **d–f** WM-10 K/s, **g–i** WM-30 K/s, **j–l** WM-150 K/s, **m–o** BM-30 K/s

temperature residence time. In this experiment, these two parameters were the same at different cooling rates, so the PAGB size was basically the same. The acicular ferrite in the welds was nucleated on the inclusion as the nucleation point. According to the calculation of the weld composition by Thermo-Calc software, the inclusion was mainly composed of Ti_2O_3 and Al_2O_3, which was also proved by our previous tests [11] (Fig. 3n). The statistic results show that the inclusion size and density were 1.5 μm and 1.2×10^5 mm^{-3}, respectively. The size and
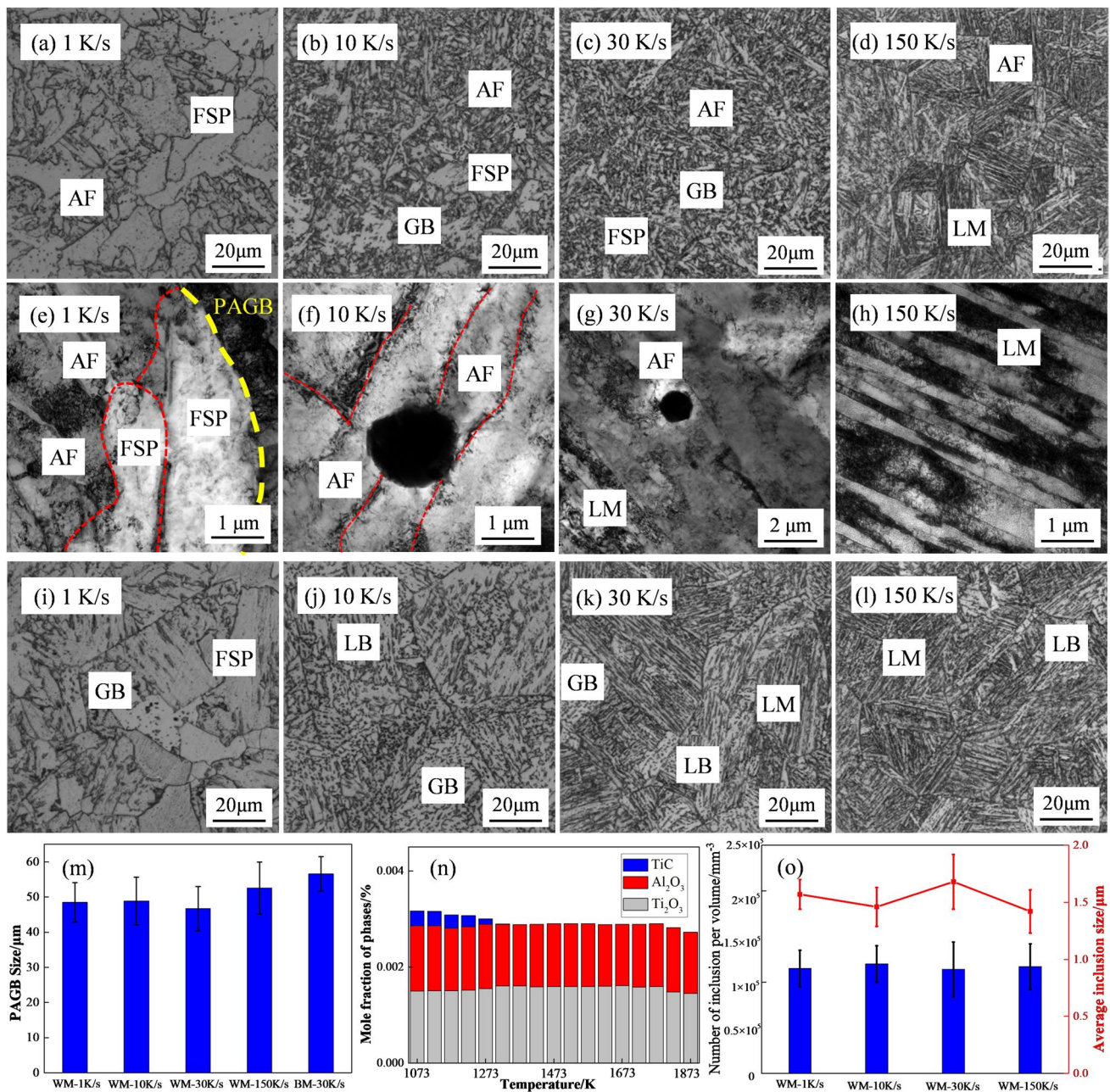
Fig. 3 Microstructure of welds at different cooling rates **a–d** OM of welds, **e–h** TEM of welds, **i–l** OM of BM, **m** the statistical results of PAGB in welds and base metal, **n** thermodynamic analysis of the evolution of inclusions in welds, **o** statistics of the number and size of inclusions

density of inclusions were at the same level at different cooling rates.

3.2 Phase Diagrams and Growth Kinetics of AF at Different Cooling Rates

The microstructural proportion of the welds at different cooling rates are shown in Fig. 4. In this study, the proportion of microstructure were determined by point counting using the IPP software and the definition of microstructure

here corresponds to previous work on low alloy steels [11, 12, 17]. In the welds, the AF fraction first increased and then decreased with the increase of cooling rates. The AF fraction was the highest (70%) at 30 K/s. The continuous cooling transformation (CCT) curve could reveal the phase transformation temperature range, thereby explaining the variation trend of the microstructure proportion with the cooling rate. Based on the field observations and microstructure statistics, the CCT curves of the weld metal and base metal were drawn, as shown in Fig. 4a, b. Both the
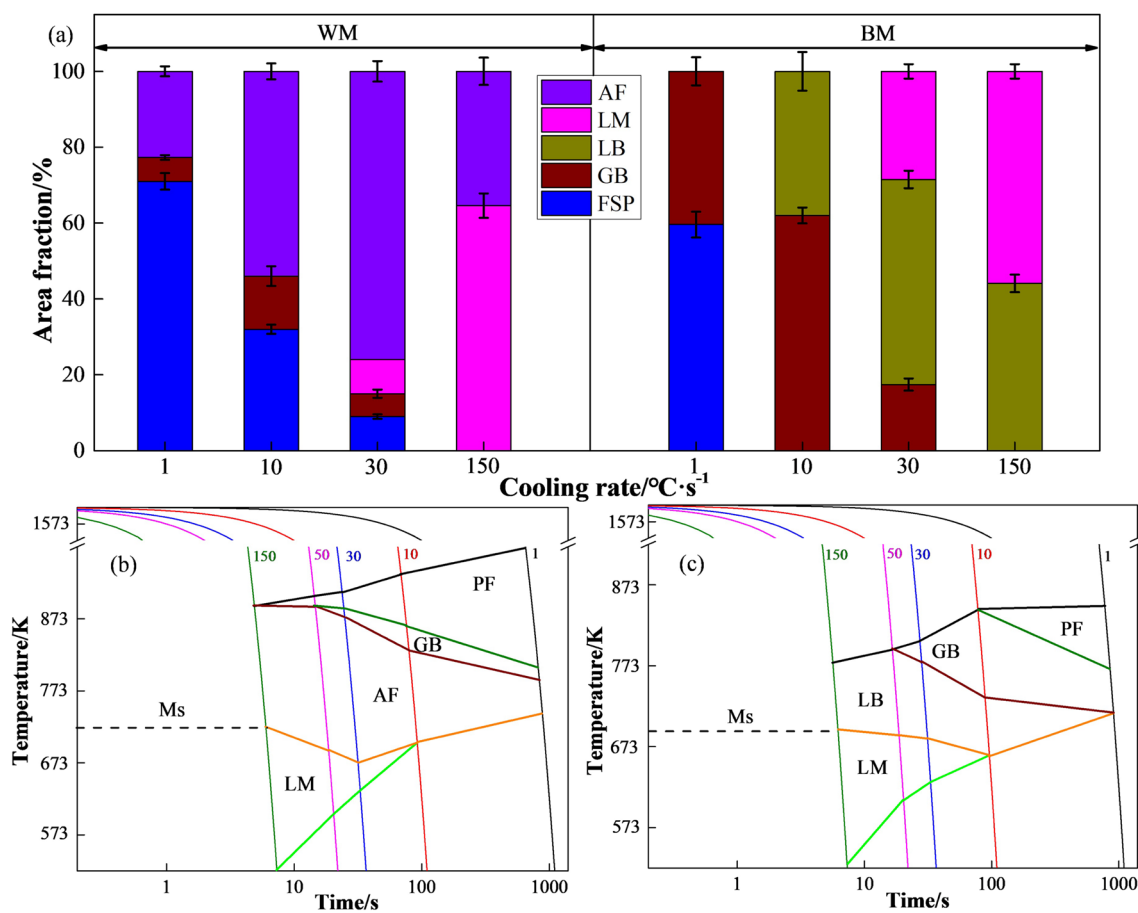
Fig. 4 Area fraction of microstructural constituent and welding CCT curves of WM and BM. **a** Area fraction of microstructural constituent, **b** WM, **c** BM

phase transformation starting and termination temperatures decreased with increasing cooling rate. This was because that the high cooling rate led to a high degree of undercooling and improved the stability of the austenite. For the weld metal, when the phase transformation termination temperature was higher than martensite starting temperature (M_s) (1–30 K/s), the area of AF phase zone gradually increased with the increase of cooling rate. However, when the phase transformation termination temperature was lower than M_s (~30 K/s), the AF phase zone gradually decreased with the increasing cooling rate. Compared with the base metal, the starting temperature of the weld metal was higher. The LB phase zone disappeared and the AF phase zone formed.

To clarify the relationship between cooling rate and AF growth rate, 5 AF slabs were selected at different cooling rate. The growth length of AF was measured. Figure 5 shows kinetic analysis of AF growth in HT-CLSM experiment. The statistical results showed that the length of AF was linearly related to the growth time of AF, indicating that the driving force of the AF phase transformation remained basically constant with time in a certain temperature range. At 1 K/s,

the growth length of AF was short, and the corresponding growth rate was about 6.35–16.62 μm/s (Fig. 5a). The growth rate of AF increased significantly with the cooling rate. At 150 K/s, the growth rate of AF reached 21–63 μm/s (Fig. 5d).

3.3 EBSD Analysis

Figure 6 shows the IPF map, grain boundary distribution map and orientation distribution map of welds and base metal. Figure 7 shows grain boundary distribution statistical results of weld and base metal. According to the statistical results of grain boundary distribution, the WM-30 K/s sample had the highest proportion of high-angle grain boundaries. Previous studies have shown [22, 23] that high-angle grain boundary was an important indicator for evaluating the impact toughness because they can greatly hinder crack propagation. The grain boundary density and grain boundary type were closely related to the variant selection and pairing, so it was necessary to study the variant selection and pairing of microstructure. The PAGBs and corresponding
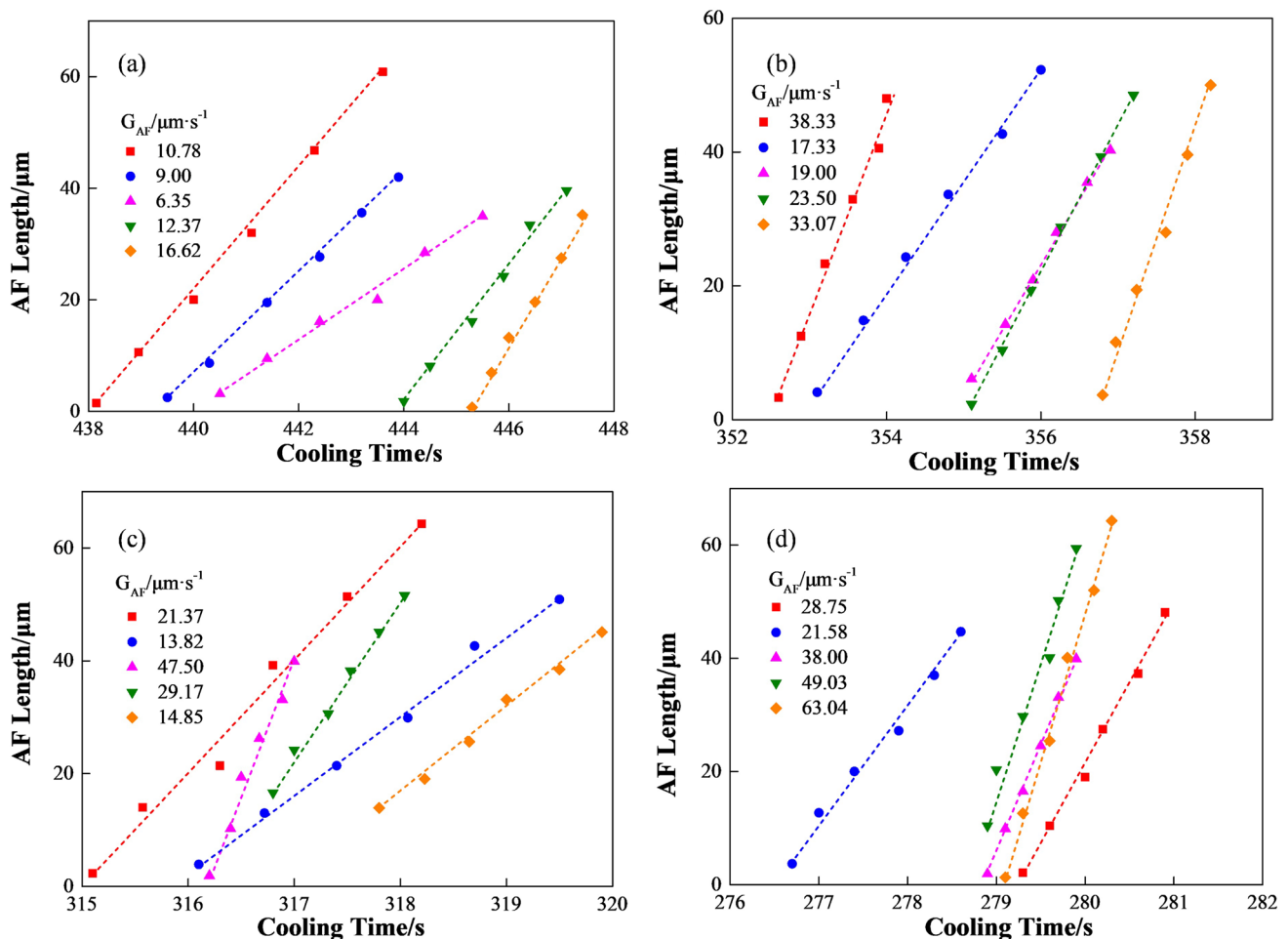
Fig. 5 Results of AF growth kinetic analysis. **a** WM-1 K/s, **b** WM-10 K/s, **c** WM-30 K/s, **d** WM-150 K/s

variant obtained by reconstructing the PAG grains are shown in Fig. 6a, d, g, j. The PAGB grain size of the WM-1 K/s was significantly smaller than other specimens. However, the PAGB size of at different cooling rates was roughly the same in Fig. 3. The reconstruction of PAGB was based on the relationship of G-T and K-S [24]. If there was no orientation relationship between the new phase and the parent phase during a phase transformation, the reconstruction accuracy of the PAG would be low and it was meaningless to study variant selection and pairing under such conditions. Figure 6c, f, i, l show the orientation images, where the color represents the relationship between the parent phase and the new phase while the black represents no relationship. There was almost no orientation relationship between the parent phase and the new phase of the WM-1 K/s sample, which was since the cooling rate was too low and the phase transformation type was a complete diffusion type transformation. It was also proved that WM-1 K/s sample had more proportion of grain boundary in none relationship zone, as shown in the black box area of Fig. 7. Therefore, in this

study, G1, G2 and G3 was selected from each of the other three samples (WM-30 K/s, WM-150 K/s and BM-30 K/s) for the study of variant selection and pairing.

Figure 8 shows the IPF figures, pole figures, CP group figures and bain figures of G1, G2 and G3. The corresponding statistics of variant and operating factor are showed in Fig. 9. For variant selection, all 24 variants were present in G1, G2 grains. While many variants (V9, V13, V15, V17) were absent in G3 grains, which had been circled in red. The variant selection were gradually heavier from G1 to G3, as evidenced by the corresponding statistical results in Fig. 9. Since the proportion of AF from G1 to G3 decreased sequentially, and previous studies have shown that bainite and martensite had heavy variant selections [25]. It can be concluded that the variant selection of acicular ferrite was relatively light compared to other types of microstructure, which meant AF tended to form all kinds of variants during the phase transformation.

For the variant pairings, the proportion of operating factors were almost the same in G1, while the proportion
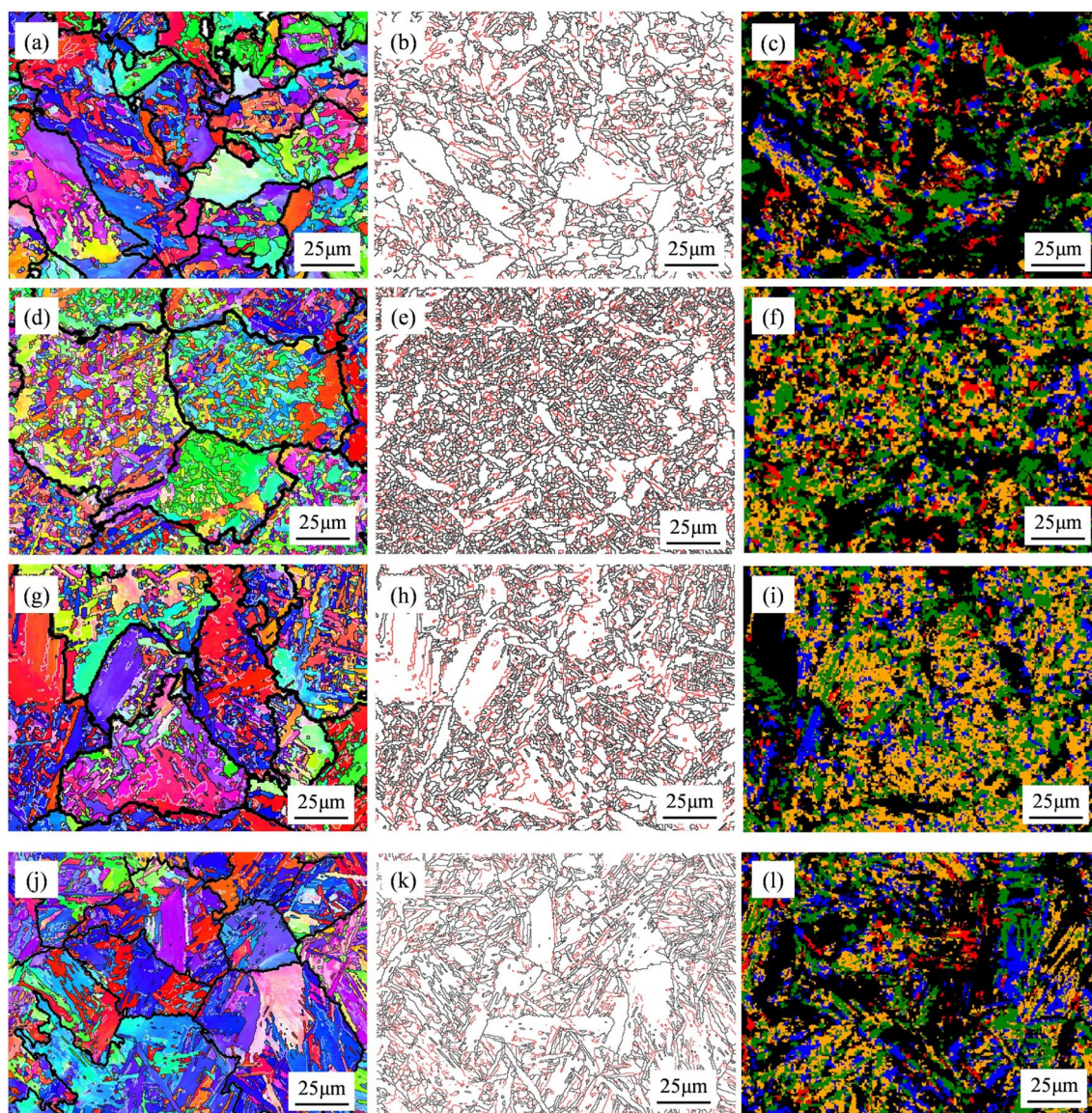
Fig. 6 IPF, grain boundary distribution map and orientation distribution map of weld and base metal **a–c** WM-1 K/s, **d–f** WM-30 K/s, **g–i** WM-150 K/s, **j–l** BM-30 K/s; IPF map (**a**, **d**, **g**, **j**), grain boundary distribution map (**b**, **e**, **h**, **k**), orientation distribution map (**c**, **f**, **i**, **l**) (red lines: $5° < θ < 15°$, black lines: $15° < θ$, θ: misorientation)

of operating factors 2 and 3 were significantly higher than the other operating factors in G2 (Fig. 9). Whereas in G3, the proportions of the operating factors are significantly different. The operating factors 2–5 were significantly higher than the other operating factors i.e. variants within the same CP group were more likely to pair together. The bain and CP group distribution maps for individual grains could illustrate the variant pairings. In G3, variants of the same CP group tended to be distributed adjacently. In G1 and G2, this situation did not appear, which showed that AF had the characteristic of uniform distribution of operating factors. In addition, the packet and block sizes of G1 grains were much smaller than G2 and G3, which was

related to the size of the variants. To improve statistical accuracy, Fig. 9c shows the grain boundary distribution for different operating factors over the entire scan range. The distribution trend of the operating factor grain boundary density was consistent with the results in Fig. 9b, which proved the accuracy of the experimental results. The grain boundary density of the WM-30 K/s specimen was higher than the WM-150 K/s and BM-30 K/s samples, which was also attributed to the small variant size of the AF. In conclusion, AF had the characteristics of light variant selection, uniformly distributed operating factor and small variant size.

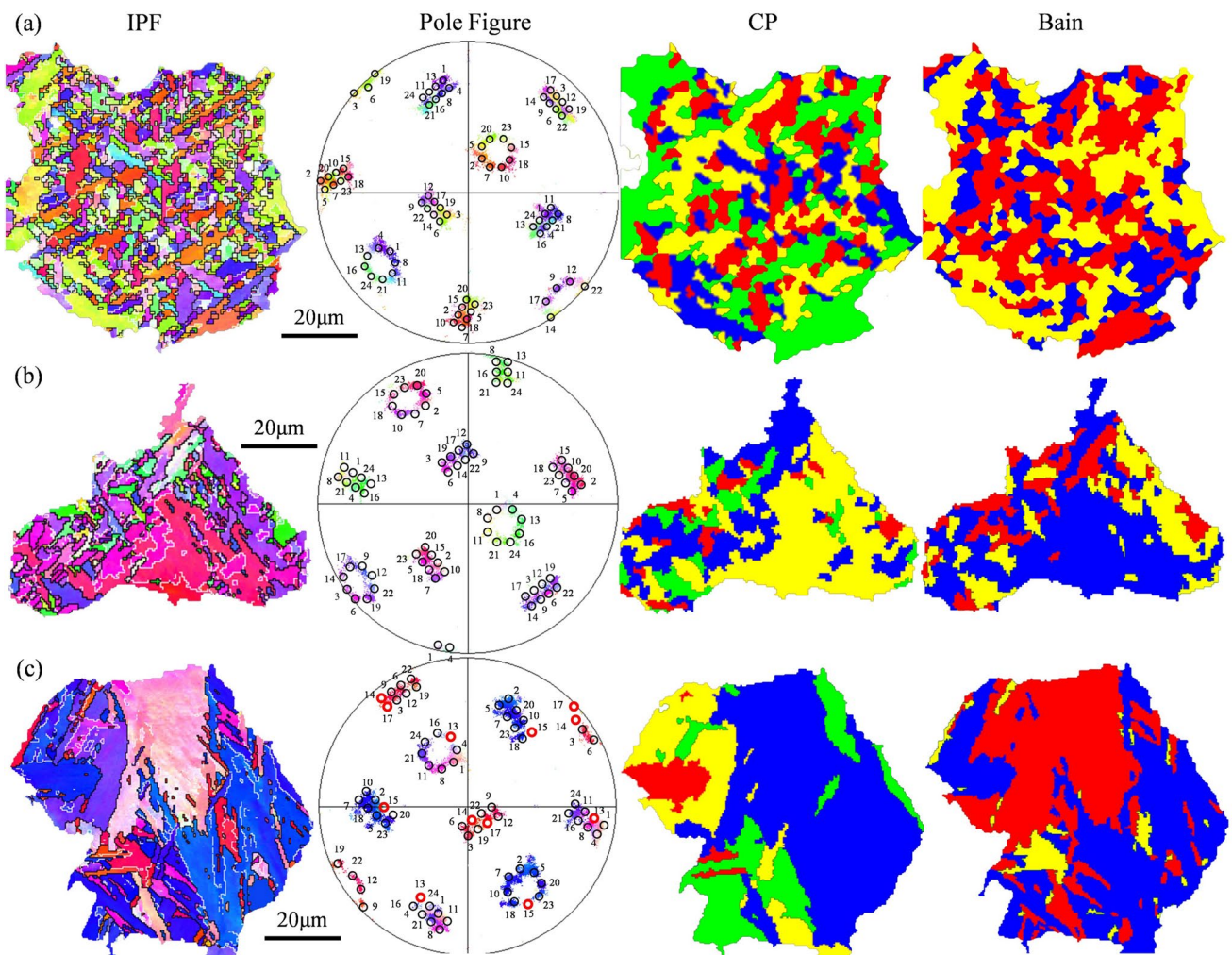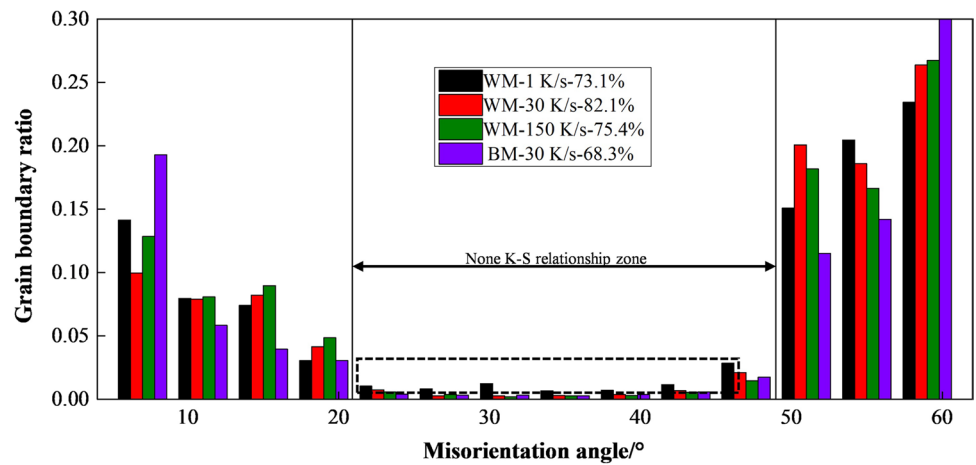**Fig. 7** The grain boundary distribution statistical results of weld and base metal

Fig. 8 IPF diagram, pole diagram, CP group diagram and Bain diagram of G1, G2 and G3 in three samples of WM-30 K/s, WM-150 K/s and BM-30 K/s **a** G1, **b** G2, **c** G3
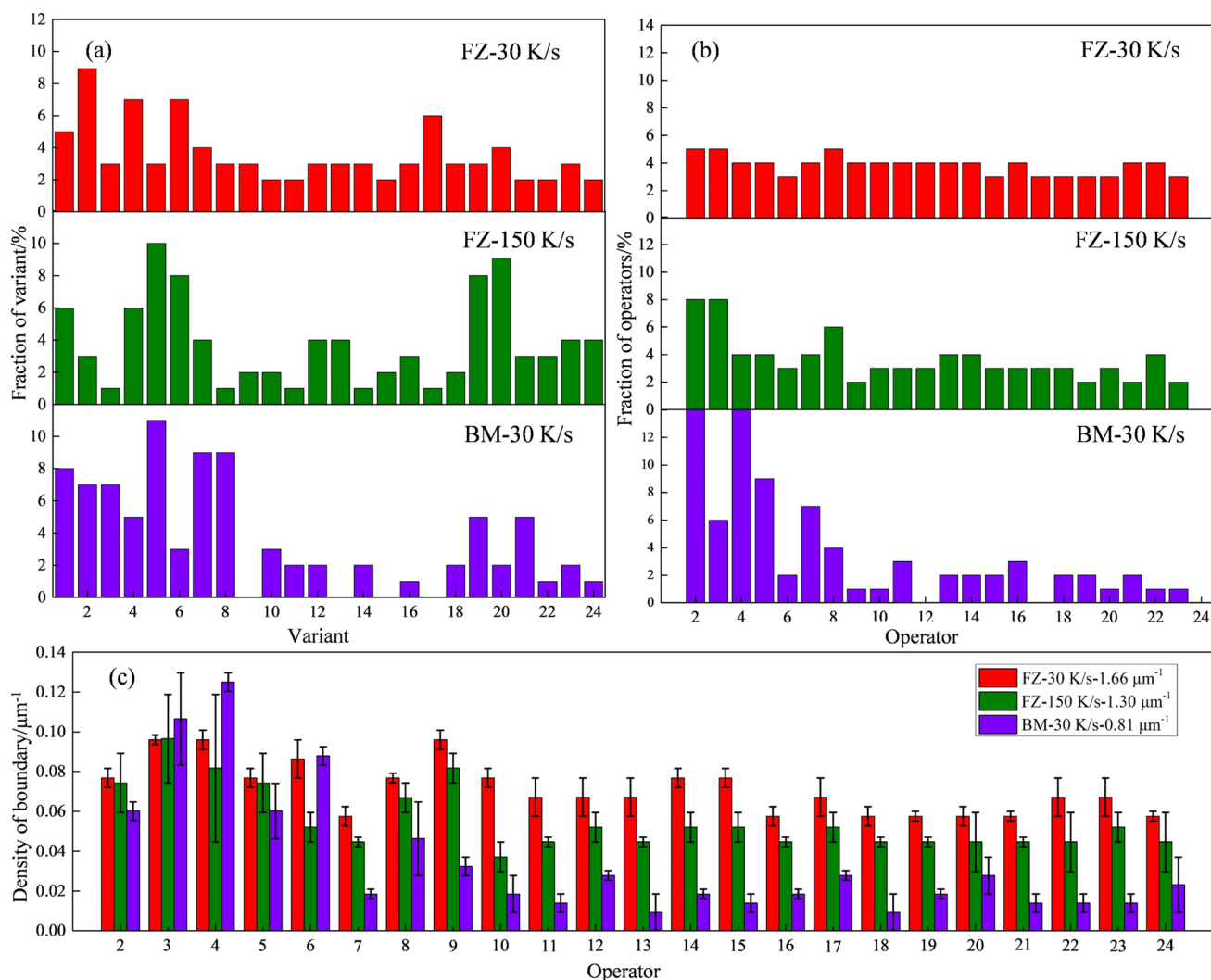
Fig. 9 Variant and operating factor statistics of G1, G2 and G3 **a** variant area fraction statistics, **b** operating factor proportion statistics, **c** grain boundary density statistics

4 Results

4.1 *In-Situ* Nucleation and Thermodynamics of AF

As described in Sect. 3.2, due to the formation of AF, the onset transformation temperature of welds reduced and LB phase zone was replaced by AF phase zone, which would be discussed in this section. During welding, shielding gas and welding wire enter the molten pool. The oxygen in the shielding gas combines with the metal elements in the molten pool to form inclusions, and the welding wire changes the chemical composition of the weld after melting into the molten pool. It can be seen from Table 1 that the content of ferrite promoting elements such as Si, Nb and Ti in the chemical composition of the welding wire is higher than the base metal, while the content of ferrite inhibiting elements such as Mn and Ni is lower than

the base metal. This results in the weld being more prone to phase transformation at high temperature to form FSP and AF. Therefore, the onset temperature of weld metal transformation is higher than the base metal. It can be seen from Fig. 6 that the phase transformation temperature ranges of AF and LB are highly coincident. Therefore, they are in a competitive relationship in the phase transformation process. The nucleation temperature of AF is higher than LB, so austenite nucleated preferentially on inclusions during cooling. The manganese-poor zone formed around the inclusions improved the driving force and promoted the transformation to form acicular ferrite at high temperature conditions [26]. The nucleation and growth of AF inhibited the nucleation of LB on austenite. Therefore, the AF phase zone replaced the LB phase zone in the weld CCT curve.

4.2 Growth Kinetics of AF

In previous studies, except for cooling rate, the PAGB size and the size and density of inclusion all affected AF nucleation. As shown in Fig. 3m–o, the PAGB size and the type, size and density of inclusion in welds at different cooling rates were at the same level. As a result, the difference in the cooling rates results in the variety of AF proportion.

It can be seen from the phase diagram that the phase transformation temperature range of AF is wide (620 K-M_s). Above the M_s, the higher the cooling rate, the higher was the AF proportion. When the phase transformation temperature was below the M_s, the higher the cooling rate, the lower was the AF fraction. As described in Sect. 3.2, the growth rate of ferrite was positively correlated with the cooling rate. Literature reports indicated that the growth mode of ferritic transformation was controlled by thermodynamic conditions, diffusivity of alloying elements, and interfacial mobility [27, 28]. According to whether alloy elements can diffuse at the interface between austenite and ferrite, the growth of austenite to ferrite can occur in two different modes (1) substitute elements (e.g. Mn) can diffuse between austenite and ferrite, and the interface is in a completely local equilibrium condition (Partitioning Local Equilibrium, PLE) and (2) substituting elements cannot diffuse but interstitial elements (e.g. C) can diffuse and the interface is in a completely local equilibrium condition (Negligible Partitioning Local Equilibrium, NPLE) [29].

The mode of ferrite growth can be appraised using the equilibrium phase diagram. Through the single point equilibrium mode in Thermo-Calc software, the phase transformation points of welds varying with carbon content and manganese content were calculated and fitted to draw the phase diagram. Mn and C were selected because they were the main substitute elements and interstitial elements in the weld, respectively. In addition to the above two elements, other elements used in the calculation are the same as those of the welds. Figure 10 shows phase diagram with PLE/NPLE mode of welds. At 823 K, austenite transformed in NPLE mode, while austenite transformed in PLE mode at 923 K. The PLE mode was characterized by a slow phase transformation rate due to the diffusion of substitutional elements during ferrite growth, while under NPLE mode ferrite growth was faster. In addition, the nucleation rate of ferrite at 923 K was lower than that at 823 K due to the lower driving force. Therefore, when the transformation termination temperature was higher than the M_s, the increase in the phase transformation rate led to an increase in the AF proportion as the cooling rate increased. When the transformation termination temperature was lower than the M_s, microstructure underwent shearing to form lath martensite. The AF ratio decreased as the cooling rate increased when the cooling rate exceeded 30 K/s. In summary, to obtain more AF, the cooling rate should be increased as much as possible on the premise that the phase transformation termination temperature is higher than the M_s.

4.3 Crystallographic Structure of AF

Previous studies have shown that the phase transformation temperature of martensite and bainite significantly affects variant selection. Wang et al. emphasized that plastic-accommodation dominated at high temperatures, and a small number of variants were formed during phase transformation due to low interfacial energies [30, 31]. Therefore, the high transformation temperature was beneficial to the variant selection of low carbon steel. While self-accommodation dominated at low transformation temperatures, which
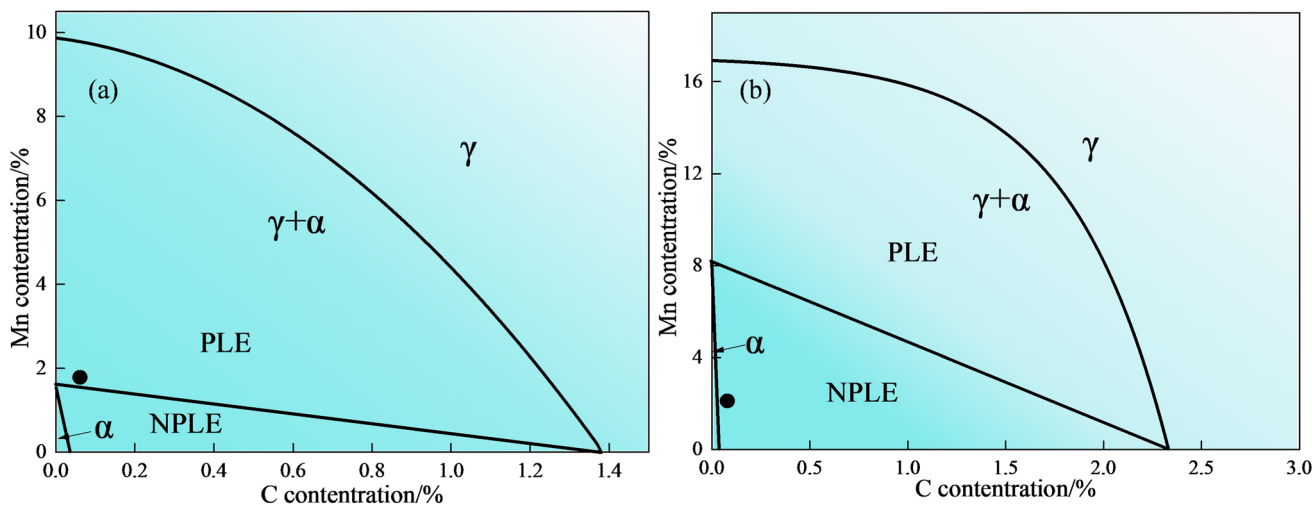

Fig. 10 Phase diagram with PLE/NPLE mode of welds (The dot gives the composition of the steel used in this study) **a** 923 K and **b** 823 K

tended to form multiple variants [32]. In conclusion, previous results showed that variant selection became weaker as the phase transformation temperature decreased. However, the order of phase transformation temperature was G1 > G2 > G3 and the order of variant selection strength was G1 < G2 < G3. The results were completely inconsistent with the previous results. The inconsistent results were attributed to the crystallographic features of AF. The nucleation position of martensite or bainite was PAGB, and the transformation product grew toward the intragranular after nucleation. Subsequent phase transformation products took the phase transformation product formed earlier as the nucleation point, so the variant formed first in the phase transformation process affected the variant formed later through plastic-accommodation mechanism or self-accommodation, and finally caused the variant selection. Whereas AF nucleated on inclusions and grew until encountering. The variants of different AFs did not affect each other, thus, there was almost no variant selection in AF, which can be proved by the statistical results of variants. Therefore, the formation of variants in AF was random.

For variant pairing, previous studies have shown that variant pairing is closely correlated to transformation strain [33]. Transformation strain generated during shear transformation was stored in transformation products. Morito [25] indicated that the formation of all six variants in the same CP group can accommodate greater transformation strain. Therefore, the variants in the same CP group were formed adjacent to each other in G3 without present of AF. The nucleation mechanism of AF resulted in a completely different variant pairing from the bainite. Studies have shown [34] that AFs nucleated by the same inclusion belong to the same Bain group. The AF grains nucleated by the same inclusion were not adjacent to each other because of the interlocking structure and morphology. Also, the orientation relationship between different inclusions was random, so the proportion of different operating factors was uniform. The operating factors formed between most AF were high-angle grain boundaries, which increased the high-angle grain boundary density.

In previous findings [35], the grain size was determined by the size of the block composed of variants in the same Bain group. If the variants of the same packet tended to be distributed adjacently, then the variants of the same Bain group would be separated and smaller size blocks would be obtained. Even so, a block would contain several variants. The variant selection and pairing characteristics in the AF led to the smallest unit affecting the effective grain boundary density being the variant. And the size of the variant in G1 was significantly smaller than G2 and G3, which is related to a needle-like interlocking structure in three-dimensional morphology of the AF. Whereas bainite and martensite were parallel bundled structures, which led to large variant sizes.

In conclusion, compared with the bainite and martensite in the base metal, the acicular ferrite had the characteristics of light variant selection, uniformly distributed operating factor and small variant size, these crystallographic structure characteristics led to its high-density effective grain boundaries.

5 Conclusion

1. Acicular ferrite can nucleate in weld metal at all the test cooling rates, and the microstructure coexisting with acicular ferrite changes from FSP and granular bainite with a low cooling rate to lath martensite with a high cooling rate. Compared with base metal, due to the formation of AF, the onset temperature of weld metal transformation is reduced and the LB phase region disappears.
2. As the cooling rate increases, the phase transformation temperature of acicular ferrite decreases, and the phase transformation mode changes from PLE to NPLE. The change of the phase transformation mode and the higher phase transformation driving force lead to an increase in the growth rate of acicular ferrite.
3. To obtain more AF, the cooling rate should be increased as much as possible on the premise that the phase transformation termination temperature is higher than the M_s.
4. Compared with the bainite and martensite in the base metal, the acicular ferrite has the characteristics of light variant selection, uniformly distributed operating factor and small variant size, these crystallographic structure characteristics lead to its high-density effective grain boundaries.

Data Availability All data generated or analyzed during this study are included in this article.

Declarations

Conflict of interest The authors declare that they have no known competing financial interests or personal relationships that could have appeared to influence the work reported in this paper.

References

1. T. Yamada, H. Terasaki, Y.I. Komizo, Relation between inclusion surface and acicular ferrite in low carbon low alloy steel weld. Trans. Iron Steel Inst. Jpn. **49**(7), 1059–1062 (2009)

2. Y. Kang, K. Han, J.H. Park, C. Lee, Mn-depleted zone formation in rapidly cooled high-strength low-alloy steel welds. Metall. Mater. Trans. A **45**(11), 4753–4757 (2014)

3. A. Takada, Y.-I. Komizo, H. Terasaki, T. Yokota, K. Oi, K. Yasuda, Crystallographic analysis for acicular ferrite formation in low carbon steel weld metals. Weld. Int. **29**(4), 254–261 (2014)

4. B. Wang, X. Liu, G. Wang, Inclusion characteristics and acicular ferrite nucleation in Ti-containing weld metals of X80 pipeline steel. Metall. Mater. Trans. A **49**(6), 2124–2138 (2018)

5. J.S. Byun, J.H. Shim, Y.W. Cho, D.N. Lee, Non-metallic inclusion and intragranular nucleation of ferrite in Ti-killed C-Mn steel. Acta Mater. **51**(6), 1593–1606 (2003)

6. H.S. Kim, H.-G. Lee, K.-S. Oh, Precipitation behavior of MnS on oxide inclusions in Si/Mn deoxidized steel. Met. Mater. **6**(4), 305–310 (2000)

7. D.S. Sarma, A.V. Karasev, P.G. Jönsson, On the role of non-metallic inclusions in the nucleation of acicular ferrite in steels. ISIJ Int. **49**(7), 1063–1074 (2009)

8. X. Wang, C. Wang, J. Kang, G. Yuan, R.D.K. Misra, G. Wang, An in-situ microscopy study on nucleation and growth of acicular ferrite in Ti–Ca–Zr deoxidized low-carbon steel. Mater. Charact. **165**, 110381 (2020)

9. X. Zou, J. Sun, H. Matsuura, C. Wang, In situ observation of the nucleation and growth of ferrite laths in the heat-affected zone of EH36-Mg shipbuilding steel subjected to different heat inputs. Metall. Mater. Trans. B **49**(5), 2168–2173 (2018)

10. Y. Yang, D. Zhan, H. Lei, G. Qiu, Y. Li, Z. Jiang, H. Zhang, In situ observation of acicular ferrite nucleation and growth at different cooling rate in Ti–Zr deoxidized steel. Metall. Mater. Trans. B **50**(6), 2536–2546 (2019)

11. X. Qi, X. Wang, H. Di, X. Shen, Z. Liu, P. Huan, L. Chen, Effect of Ti content on the inclusions, microstructure and fracture mechanism of X100 pipeline steel laser-MAG hybrid welds. Mater. Sci. Eng. A **831**, 142207 (2022)

12. X. Qi, P. Huan, X. Wang, X. Shen, Z. Liu, H. Di, Effect of microstructure homogeneity on the impact fracture mechanism of X100 pipeline steel laser-MAG hybrid welds with an alternating magnetic field. Mater. Sci. Eng. A **851**, 143656 (2022)

13. W.L. Costin, O. Lavigne, A. Kotousov, A study on the relationship between microstructure and mechanical properties of acicular ferrite and upper bainite. Mater. Sci. Eng. A **663**(29), 193–203 (2016)

14. H. Zhao, B.P. Wynne, E.J. Palmiere, Conditions for the occurrence of acicular ferrite transformation in HSLA steels. J. Mater. Sci. **53**(5), 3785–3804 (2018)

15. X.L. Wan, K.M. Wu, K.C. Nune, Y. Li, L. Cheng, In situ observation of acicular ferrite formation and grain refinement in simulated heat affected zone of high strength low alloy steel. Sci. Technol. Weld. Join. **20**(3), 254–263 (2015)

16. F. Liu, J. Li, Q. Wang, Y. Liu, Y. Bai, T. He, G. Yuan, Microstructural refinement by the formation of acicular ferrite on Ti–Mg oxide inclusion in low-carbon steel. Mater. Sci. Eng. A **824**(8), 141795 (2021)

17. X. Qi, X. Wang, H. Di, X. Shen, P. Huan, J. He, L. Chen, Acicular ferrite nucleation mechanism in laser-MAG hybrid welds of X100 pipeline steel. Mater. Lett. **304**, 130603 (2021)

18. G. Miyamoto, N. Iwata, N. Takayama, T. Furuhara, Mapping the parent austenite orientation reconstructed from the orientation of martensite by EBSD and its application to ausformed martensite. Acta Mater. **58**(19), 6393–6403 (2010)

19. P. Zhou, B. Wang, L. Wang, Y. Hu, L. Zhou, Effect of welding heat input on grain boundary evolution and toughness properties in CGHAZ of X90 pipeline steel. Mater. Sci. Eng. A **722**(11), 112–121 (2018)

20. L. Lan, X. Kong, C. Qiu, Characterization of coarse bainite transformation in low carbon steel during simulated welding thermal cycles. Mater. Charact. **105**, 95–103 (2015)

21. L. Lan, C. Qiu, D. Zhao, X. Gao, L. Du, Microstructural characteristics and toughness of the simulated coarse grained heat affected zone of high strength low carbon bainitic steel. Mater. Sci. Eng. A **529**(25), 192–200 (2011)

22. Y.S. Yu, Z.Q. Wa Ng, B.B. Wu, J.X. Zhao, X.L. Wa Ng, H. Guo, C.J. Shang, Tailoring variant pairing to enhance impact toughness in high-strength low-alloy steels via trace carbon addition. Acta Metall. Sin. (Engl. Lett.) **34**(6), 755–764 (2021)

23. X. Qi, P. Huan, X. Wang, H. Di, X. Shen, Q. Sun, Z. Liu, J. He, Study on the mechanism of heat input on the grain boundary distribution and impact toughness in CGHAZ of X100 pipeline steel from the aspect of variant. Mater. Charact. **179**, 111344 (2021)

24. M.X. Zhang, P.M. Kelly, Accurate orientation relationship between ferrite and austenite in low carbon martensite and granular bainite. Scr. Mater. **47**(11), 749–755 (2002)

25. S. Morito, H. Tanaka, R. Konishi, T. Furuhara, T. Maki, The morphology and crystallography of lath martensite in Fe–C alloys. Acta Mater. **51**(6), 1789–1799 (2003)

26. Y. Kang, S. Jeong, J. Kang, C. Lee, Factors affecting the inclusion potency for acicular ferrite nucleation in high-strength steel welds. Metall. Mater. Trans. A **47**(6), 2842–2854 (2016)

27. H. Farahani, W. Xu, S. van der Zwaag, Prediction and validation of the austenite phase fraction upon intercritical annealing of medium Mn steels. Metall. Mater. Trans. A **46**(11), 4978–4985 (2015)

28. Z.Q. Liu, G. Miyamoto, Z.G. Yang, T. Furuhara, Direct measurement of carbon enrichment during austenite to ferrite transformation in hypoeutectoid Fe–2Mn–C alloys. Acta Mater. **61**(8), 3120–3129 (2013)

29. A.M. Ravi, A. Kumar, M. Herbig, J. Sietsma, M.J. Santofimia, Impact of austenite grain boundaries and ferrite nucleation on bainite formation in steels. Acta Mater. **188**(15), 424–434 (2020)

30. X.L. Wang, Z.Q. Wang, L.L. Dong, C.J. Shang, X.P. Ma, S.V. Subramanian, New insights into the mechanism of cooling rate on the impact toughness of coarse grained heat affected zone from the aspect of variant selection. Mater. Sci. Eng. A **704**(17), 448–458 (2017)

31. B.B. Wu, Z.Q. Wang, X.L. Wang, W.S. Xu, C.J. Shang, R. Misra, Toughening of martensite matrix in high strength low alloy steel: regulation of variant pairs. Mater. Sci. Eng. A **759**(24), 430–436 (2019)

32. N. Takayama, G. Miyamoto, T. Furuhara, Effects of transformation temperature on variant pairing of bainitic ferrite in low carbon steel. Acta Mater. **60**(5), 2387–2396 (2012)

33. G.M. Xie, R.H. Duan, Y.Q. Wang, Z.A. Luo, C. Wang, G.D. Wang, Crystallography of the nugget zone of bainitic steel by friction stir welding in various cooling mediums. Mater. Charact. **182**, 111523 (2021)

34. H. Nako, H. Hatano, Y. Okazaki, K. Yamashita, M. Otsu, Crystal orientation relationships between acicular ferrite, oxide, and the austenite matrix. ISIJ Int. **54**(7), 1690–1696 (2014)

35. Z. Guo, C.S. Lee, J.W. Morris Jr., On coherent transformations in steel. Acta Mater. **52**(19), 5511–5518 (2004)